Synergistic effect of surface oxygen vacancies and interfacial charge transfer on Fe(III)/Bi_2MoO_6 for efficient photocatalysis

Feng Fu,[a] *Huidong* Shen,a Xiang Sun,b Wenwen Xue,a Ayoola Shoneye,c Jiani Ma,d Lei Luo,d Danjun Wang,*a Jianguo Wang,*b and Junwang Tang*c

aCollege of Chemistry & Chemical Engineering, Yan'an University, Shaanxi Key Laboratory of Chemical Reaction Engineering, Yan'an 716000, China.

bInstitute of Industrial Catalysis, State *Key Laboratory Breeding Base of Green-Chemical Synthesis Technology, College of Chemical Engineering, Zhejiang University of Technology, Hangzhou 310032, P.R. China*

[c]*Department of Chemical Engineering, University College London, Torrington Place, London WC1E 7JE, UK.*

[d]*Key Lab of Synthetic and Natural Functional Molecule Chemistry of Ministry of Education, and the Energy and Catalysis Hub, College of Chemistry and Materials Science, Northwest University, Xi'an 710069, P. R. China*

***Corresponding author 1: Danjun Wang**

E-mail: wangdj761118@163.com

***Corresponding author 2: Jianguo Wang**

E-mail: jgw@zjut.edu.cn

***Corresponding author 3: Junwang Tang**

E-mail: junwang.tang@ucl.ac.uk

Abstract: Novel Fe(III) clusters grafted Bi2MoO6 nanosheets with surface oxygen vacancies (denoted as F/BMO-SOVs) heterostructured composite have been firstly fabricated via a reliable

calcination process combined with impregnation approach. The surface oxygen vacancies (SOVs) in Bi_2MoO_6 were formed due to controlled calcination process. The presence of Fe (III) clusters was confirmed by HRTEM, XPS, and UV-Vis DRS. Under visible light irradiation, the optimum molar ratio of 15% F/BMO-SOVs achieved 93.4% degradation efficiency of phenol within 180 min, representing nearly 80 times higher activity than the pure Bi_2MoO_6, confirmed by both absorption spectrum and TOC measurement. The dramatically enhanced photocatalytic activity is attributed to the synergistic effect between the SOVs, Fe(III) clusters and Bi_2MoO_6, which not only narrows the band gap, improving the visible light response ability, but also facilitates the direct interfacial charge transfer (IFCT) from the SOVs to the surface Fe(III) clusters, greatly promoting the efficient separation of photogenerated electron-hole pairs. According to the trapping experiments and ESR measurements results, $\cdot O_2^-$, $\cdot OH^-$, and h^+ all participated in the phenol photodegradation process over F/BMO-SOVs. Thus this work not only provides a synergistic effect between SOVs, Fe(III) clusters and Bi_2MoO_6 involving an IFCT process, but also proposes an efficient approach to fabricating highly active photocatalysts in environmental remediation and solar fuel synthesis.

Keywords: Heterostructured Fe(III)/Bi_2MoO_6, Surface oxygen vacancy, Interfacial charge transfer, Synergistic effect, Phenol degradation

1. Introduction

Phenol and phenolic compounds in water bodies have been listed as a class of priority pollutants by the United States Environmental Protection Agency (USEPA), because of their persistence and high toxicity, and could cause respiratory, nervous and cardiovascular problems to human beings [1-3]. The World Health Organization (WHO) has also strictly regulated total phenols concentration below 0.5 $\mu g \cdot L^{-1}$ for drinking water [2]. Therefore, it is highly desirable to develop effective technologies to further eliminate phenol and phenolic compounds in water.

In consideration of solar energy conversion, semiconductor-based photocatalysis has been viewed as one of the most promising green technology for the removal of phenol and phenolic compounds from aqueous media [4, 5]. Among various semiconductor materials, Bi-based semiconductors such as Bi_2WO_6 and Bi_2MoO_6, belonging to the Aurivillius family, have received considerable scientific research interest due to their layered structures and high catalytic properties [6, 7]. In particular, Bi_2MoO_6 is a photocatalyst with band gap of 2.5~2.8eV, and is nontoxic, highly photostable, thermally stable and eco-friendly. Recently, Zhu et al. [8] revealed that Bi_2MoO_6 may be a potential candidate as one of the most promising visible light-driven photocatalyst for degradation of organic pollutants in wastewater. Nonetheless, the overall solar energy conversion efficiency remains limited by visible-light responsive region, the relatively rapid recombination of photoexcited electron-hole pairs and slow carrier transport [9, 10].

Hence, it is imperative to explore effective ways to further extend the range of visible-light response and improve the photocatalytic activity of Bi_2MoO_6.

The introduction of surface oxygen vacancies (SOVs) is one effective approach to narrow the band gap and suppress the recombination of photogenerated charge carriers in semiconductors, in order to achieve high visible-light-driven photocatalytic activity [11]. It has been reported that SOVs with abundant localized electrons are of particular interest for the enhanced adsorption and activation of O_2 to reactive oxygen species, which could further inhibit the recombination of photo-generated charge carriers [12-15]. Recently, many researchers have reported different kinds of semiconductor-based photocatalysts, such as TiO_2, BiOBr, and $BiVO_4$, which displayed excellent visible-light photocatalytic activities [16-18]. Zhu et al. [19] reported that the introduction of SOVs in $BiPO_4$ via a solvothermal-calcination route could broaden the valence band, thus leading to an improved photocatalytic activities. Recently, Huang et al. [20] used a high pressure hydrogenation treatment process to prepare SOVs-rich $BiFeO_3$ nanocrystals. The presence of SOVs in $BiFeO_3$ resulted into a narrow band gap and also facilitated the separation of photogenerated electron-hole pairs. A similar phenomenon has also been observed on Bi_2O_3 by Lu's group [21]. However, a study based on Bi_2MoO_6 with SOVs has not been reported.

Besides the introduction of SOVs, the cationic clusters-grafting is another efficient strategy to enhance the visible-light-driven activity of semiconductor photocatalysts via interfacial charge transfer (IFCT) [22]. Currently, the grafting of cationic clusters, such as

Cu(II) and Fe(III) clusters on the surface of TiO_2, which could extend light absorption to the visible light region, and subsequently increase the photocatalytic efficiency have been reported [23-26]. This efficient strategy has also been applied to non-TiO_2 semiconductors, to enhance visible light photocatalytic activity [27-29]. For example, Qiu et al. [30] prepared efficient visible-light-driven BiOCl photocatalysts by grafting Fe(III) clusters on the surface of BiOCl microflowers through a simple impregnation method. He found that the enhancement in visible-light driven photocatalytic activity of the Fe(III)-grafted BiOCl photocatalysts was attributed to the fact that the Fe(III) clusters can facilitate the separation of photogenerated electron-hole via IFCT process under visible light irradiation. In addition, Dong et al. [31] reported that the grafting of Fe(III) clusters onto the surface of $(BiO)_2CO_3$ hierarchical structure, through the impregnation method, can enhance the photocatalytic activity of $(BiO)_2CO_3$, originating from the IFCT effect between the Fe(III) clusters and $(BiO)_2CO_3$. To the best of our knowledge, the IFCT effect of Fe(III) clusters on the surface of Bi_2MoO_6 for enhancing its photocatalytic activity has not been reported.

To achieve an optimal photocatalytic activity, the combination of above-mentioned two strategies is applied to the preparation of a composite photocatalyst, which can produce a strong synergistic effect for the efficient photodecomposition of contaminants. Herein, we report a novel F/BMO-SOVs photocatalyst that has been rationally designed and successfully fabricated via solvothermal synthesis of Bi_2MoO_6. The as-prepared Bi_2MoO_6 nanosheets with surface oxygen vacancies (denoted as BMO-SOVs) were

impregnated with Fe(III) clusters. The photocatalytic performance of the prepared composites was investigated by degrading a colorless organic model pollutant (phenol) under visible light irradiation. It is shown that the obtained F/BMO-SOVs photocatalyst demonstrated a remarkable enhancement in photocatalytic activity for degradation of phenol as compared with those of Bi_2MoO_6, BMO-SOVs, and F/BMO under visible light illumination. The highly enhanced photocatalytic efficiency observed in F/BMO-SOVs should be attributed to the synergistic effect of the SOVs and IFCT. The present work has been proven to be a new combined strategy, which is also applicable to the design and construction of other photocatalytic systems to enhance photocatalytic performance.

2. Experimental Section

2.1. Sample preparation

Preparation of Bi_2MoO_6 with surface oxygen vacancies (BMO-SOVs). All the chemicals were of analytical grade and used as received. Distilled water was used in all experiments. Bi_2MoO_6 with surface oxygen vacancies was prepared according to a procedure described in our previous work [32]. In a typical process, 1.3 mmol of $Bi(NO_3)_3 \cdot 5H_2O$ and 0.65 mmol of $Na_2MoO_4 \cdot 2H_2O$ were dispersed in 13.0 mL of ethylene glycol (EG) under vigorous stirring until a transparent solution was formed. Afterwards, 32.5 mL of ethanol was added and the mixture was stirred for another 30

min. Finally, the mixed solution was transferred into a 65.0 mL Teflon-lined stainless steel autoclave. The autoclave was sealed and maintained at 160 ℃ for 12 h. The product was separated by centrifugation and washed with deionized water three times and then dried at 60 ℃ in a vacuum oven for 12 h. The obtained product was marked as BMO. Subsequently, these products were annealing at 250 ℃ for 2 h in air with the heating rate of 2 ℃/min in order to introduce extra surface oxygen vacancies, and the resulting products were denoted as BMO-SOVs (Bi_2MoO_6 with surface oxygen vacancies).

Synthesis of Fe(III)/Bi_2MoO_6-SOVs (F/BMO-SOVs) photocatalysts. The Fe(III)/Bi_2MoO_6-SOVs photocatalyst was prepared by an impregnation technique as reported previously [31]. Specifically, 0.305 g of BMO-SOVs sample was uniformly dispersed in 50 mL distilled water via ultrasonic treatment for 30 min. The aqueous suspension was transferred into a thermostat water bath at 60 ℃ and stirred for 20 min. Afterwards, varying amounts of $Fe(NO_3)_3$ aqueous solution was slowly added into the above solution, followed by stirring at 60 ℃ for 2 h. The final product was filtered, washed several times with deionized water and ethanol, and dried at 60 ℃ for 12 h in a vacuum oven. The theoretical molar ratio of $Fe(NO_3)_3$ to BMO-SOVs was controlled at 5%, 10%, 15%, 20%, and 25%, respectively. Accordingly, the resultant product was milled into powder and labeled as 5% F/BMO-SOVs, 10% F/BMO-SOVs, 15% F/BMO-SOVs, 20% F/BMO-SOVs, and 25% F/BMO-SOVs. For comparison, 15% Fe(III)/Bi_2MoO_6 was synthesized by the same procedure, but replacing BMO-SOVs with Bi_2MoO_6, and the obtained product was labeled as 15% F/BMO. The preparation process

of F/BMO-SOVs composite is shown in **Scheme 1**.

2.2. Characterization of photocatalysts

Powder X-ray diffraction (XRD) was carried out on a Shimadzu XRD-7000 X-ray diffractometer using Cu Kα radiation (λ = 0.15418 nm) at a scanning rate of 2° min^{-1} in a 2θ range of 5° - 80°. The accelerating voltage and the applied current were 40 kV and 30 mA, respectively. X-ray photoelectron spectroscopy (XPS) was recorded on a PHI-5400 X-ray photoelectron spectrometer. Field emission scanning electron microscope (FE-SEM) images were recorded on a JSM-6700F scanning electron microscope. Energy-dispersive X-ray (EDS) spectra were obtained using a JEOL-2100 at an accelerating voltage of 200 kV. High-resolution transmission electron microscope (HRTEM) images was recorded on a JEM-2100 electron microscope operated at an accelerating voltage of 200 kV. In situ electron paramagnetic resonance (EPR) measurement was taken in an endor spectrometer (JEOL ES-ED3X). The g factor was obtained by taking the signal of manganese as standard. The electron spin resonance (ESR) signals of radicals, trapped by a spin-trap reagent DMPO (5,5′-dimethyl-1-pyrroline-N-oxide) (Sigma Chemical Co.) in water, were examined on a Bruker model ESR JES-FA200 spectrometer equipped with a Quanta-Ray Nd: YAG laser system as the irradiation source (λ ≥ 420 nm). To minimize experimental errors, the same type of quartz capillary tube was used for all ESR measurements. Raman spectra were recorded by

using a Horiba Jobin-Yvon LabRam HR800 Raman microspectrometer, with laser excitation at 320 nm. The UV-Vis diffuse reflectance spectra (UV-Vis-DRS) of the samples were obtained using Shimadzu UV-2550 UV-Vis spectrophotometer. $BaSO_4$ was used as a reflectance standard. Room-temperature photoluminescence spectra (PL) and time-resolved photoluminescence spectra (TR-PL) were detected with a Horiba FLTCSPC fluorescence spectrophotometer. Photoelectrochemical properties such as photocurrent (PC) and electrochemical impedance spectra (EIS) were performed on an electrochemical analyzer (CHI660D, CHI Shanghai, Inc.) in a standard three-electrode configuration with a Platinum wire as the counter electrode and saturated calomel electrodes (in saturated KCl) as a reference electrode [32].

2.3. Photocatalytic activity

Evaluation of the photocatalytic activities of as-prepared samples towards complete degradation of the colorless organic model pollutant (phenol) was performed as follows: A 400W halogen lamp (Nanjing XuJiang electrical and mechanical plant, Nanjing, P. R. China) with a 420 nm cut-off filter was chosen as the visible light source. A suspension containing 200 mg of photocatalyst and 200 mL of 10 $mg \cdot L^{-1}$ phenol (1.0 $g_{cat}/L_{solution}$) fresh aqueous solution were continuously stirred in the dark for 30 min to establish an adsorption/desorption equilibrium of phenol solution. After this period of time, the light source was turned on. During the reaction, a 5.0 mL sample was withdrawn at given time

intervals and the photocatalysts were then separated by centrifugation. The residual concentration of phenol in solution was estimated using absorption at 507 nm by a Shimadzu 2550 UV-visible spectrophotometer following the 4-aminoantipyrine colorimetric method [33]. Total organic carbon (TOC) in the phenol solution was recorded by automatic total organic carbon analyzer (VARIO, Elementar, Germany).

2.4 Computational details

First-principles calculations have been performed with density functional theory (DFT) as implemented in Vienna *ab initio* simulation package (VASP) [34].The Perdue-Burke-Ernzerhof (PBE) approach was adopted to describe the exchange correlation effects on the basis of the Projected Augmented Wave (PAW) method with plane wave cutoff energy of 450 eV [35]. During geometry optimization, all of the structures were relaxed until the component of force acting on each atom was smaller than 1×10^{-2} eV/Å, and the convergence of the total energy was close to 1×10^{-5} eV/cell.

The Bi_2MoO_6 of space group $Pca2_1$ was selected as computational model according to XRD. The Monkhorst-Pack Method [36] with k-points grids of $6 \times 6 \times 2$ was used for describing the Brillouin zone corresponding to supercell ($2 \times 1 \times 2$ unit cell). The oxygen defect formation energy was defined as:

$$E_{form} = E_{Bi8Mo4O23} + \mu_O - E_{Bi8Mo4O24}$$

Where $E_{Bi8Mo4O24}$, $E_{Bi8Mo4O23}$ were the total energy of $Bi_8Mo_4O_{24}$ and $Bi_8Mo_4O_{24}$, respectively. μ_O was half of the total energy of oxygen molecule.

3. Results and discussion

3.1. Structure and morphology characterization

The crystalline nature and purity of as-prepared pure BMO, BMO-SOVs, F/BMO-SOVs, and F/BMO composites were measured by XRD. As shown in **Fig. 1a**, all the identifiable diffraction peaks of BMO can be well indexed to the orthorhombic crystal structure (JCPDS card No.76-2388) and no other impurities can be detected, indicating that the calcination and impregnation processes did not markedly change the crystal structure of BMO. Compared to the pure BMO, the position of characteristic peaks of F/BMO-SOVs and F/BMO did not change, which indicates that the Fe(III) clusters were dispersed on the surface of pure BMO and BMO-SOVs instead of getting into its interlayers. Meanwhile, no diffraction peaks of Fe(III) species were detected, this was attributed to the low content and high dispersion of Fe(III) ions in the pure BMO and BMO-SOVs crystal structure. As shown in **Fig. 1b**, a slight shift of the (131) diffraction peak could be found in the enlarged XRD patterns after the calcination process due to

high temperature-induced lattice contraction [32]. The XRD patterns of the other F/BMO-SOVs (5%, 10%, 20%, 25%) samples are similar to that of 15% F/BMO-SOVs (**Fig. S1a**). The corresponding lattice parameters and cell volumes of samples are listed in **Table S1**. It is noted that the cell volumes of BMO-SOVs, F/BMO-SOVs, and F/BMO samples slightly decreased in comparison with that of BMO.

The chemical compositions and surface electronic states of as-prepared BMO, BMO-SOVs, and F/BMO-SOVs composites were investigated by XPS. The full XPS survey spectrum is presented in **Fig. S1b**. It can be seen that the Bi, O, Mo, and Fe elements could all be clearly detected with strong characteristic peaks. **Fig. 1c** and **1d** display the high-resolution Bi 4f and O 1s XPS spectra of the BMO samples. In the Bi 4f spectra, two asymmetric peaks located at 159.3 and 164.6 eV can be ascribed to Bi $4f_{7/2}$ and Bi $4f_{5/2}$, respectively, suggesting that the Bi is in the form of Bi^{3+} [37]. The corresponding peaks in the spectra of BMO-SOVs and F/BMO-SOVs shifted to 159.5 and 164.8 eV, respectively, being 0.2 eV higher than those of Bi_2MoO_6, thus implies the existence of SOVs on the surface of BMO-SOVs and F/BMO-SOVs. However, the Mo 3d spectra of samples BMO, BMO-SOVs, and F/BMO-SOVs are almost identical (**Fig. S1c**). It can be seen that two characteristic peaks of Mo $3d_{5/2}$ and Mo $3d_{3/2}$ from Mo^{6+} respectively centered at 232.5 and 235.6 eV are observed [38]. As shown in **Fig. 1d**, the O1s peak can be deconvoluted into three peaks at 529.8, 530.6, and 531.9 eV, which are ascribed to the Bi-O, Mo-O, and OH group on the surface of Bi_2MoO_6, respectively [39]. The O 1s XPS spectra of BMO-SOVs and F/BMO-SOVs shifted to a higher binding

energy from 530.20 eV to 530.48 eV (**Fig. 1d**), which are attributed to the formation of neighboring oxygen vacancies with a high electron-attracting effect [40]. As presented in **Fig. S1d**, for the Fe 2p XPS spectrum, two peaks at around 711.0 and 724.7 eV, corresponding to Fe(III) ions in amorphous Fe_2O_3 and FeOOH, are observed, and can be assigned to Fe $2p_{3/2}$ and Fe $2p_{1/2}$, respectively [41-43]. These findings clearly corroborate the composition of the obtained F/BMO-SOVs composites and the existence of oxygen vacancies.

The morphology and microstructure of the as-prepared BMO and F/BMO-SOVs were directly investigated by SEM, TEM, and HRTEM. **Fig. 2a** and **2b** show that the pure BMO sample consists of a large amount of nanosheets with a thickness of 20-50 nm. These nanosheets aggregated together to form hierarchical microspheres with average diameter of 1-2 μm. Furthermore, the morphology of F/BMO-SOVs samples (**Fig. 2c** and **2d**) are quite similar to the BMO sample, indicating that the calcination processes and Fe(III) clusters grafting does not change the morphological structure of BMO. However, some small spherical Fe(III) clusters are observed on the surface of the BMO hierarchical microspheres (inset of **Fig. 2d**), indicating a high dispersion of Fe(III) clusters. This observation is in good agreement with the XPS results. Furthermore, the corresponding EDS mapping images (**Fig. 3a-3d**) clearly demonstrated the distribution of Bi, Mo, O, and Fe elements, which gives a strong evidence that the Fe(III) clusters are uniformly distributed on the surface of BMO-SOVs.

TEM and HRTEM analysis were performed to further elucidate the morphologies and microstructures of BMO and F/BMO-SOVs. **Fig. 4a** and **4c** show the TEM images of BMO and F/BMO-SOVs, which displayed a flower-like microsphere structure. The HR-TEM images of BMO are shown in **Fig. 4b**. The lattice spacing is measured to be 0.315 nm, which corresponds to the (131) crystal plane of BMO (inset of **Fig. 4b**) [44]. High-resolution TEM image shown in **Fig. 4d** clearly indicates that the Fe(III) clusters were located on the surface of BMO-SOVs. Note that some amorphous clusters can be observed on the surface, which can be indexed as Fe(III) containing clusters. This kind of clusters have also been observed by HRTEM in Cu(II) and Fe(III)-grafted TiO_2 [23-26].

3.2. Formation of Surface Oxygen Vacancy

As shown in **Fig. 5a** and **5b**, the HRTEM image clearly reveals that both BMO and BMO-SOVs are structurally uniform. However, pure BMO sample displays a perfect lattice feature (**Fig. 5a**), but the edge of lattice fringe for BMO-SOVs becomes blurred and disordered (**Fig. 5b**), which indicates the surface structure is damaged and SOVs are formed [19]. Hence, the generation of SOVs stems from the calcination process.

To further confirm the existence of oxygen vacancies, EPR spectra analysis was performed. It can be used to directly and accurately detect the existence of oxygen vacancies in semiconductors [45]. The EPR signal curves of BMO, BMO-SOVs, F/BMO-SOVs, and F/BMO are fitted and shown in **Fig. 5c**. It can be seen that the

characteristic EPR signal with a small g-value of 1.991 was observed for BMO and F/BMO, which may be attributed to the presence of oxygen vacancies [32]. Compared to BMO and F/BMO, remarkable symmetric peaks with a g-value of around 2.004 for BMO-SOVs and F/BMO-SOVs were observed, which are typical peaks of surface oxygen vacancies [46, 47]. In addition, the intensity of EPR signal for F/BMO-SOVs is considerably stronger than that of BMO-SOVs, which was gradually enhanced with increasing SOVs' concentration [48]. This result further corroborates that the formation of SOVs on the surface of BMO was successfully produced via the thermal treatment process.

Raman spectroscopy is an effective characterization technique to further investigate the crystal defects and the distortion of crystal structure. As shown in **Fig. 5d**, all of the samples exhibit the typical vibration mode of Bi_2MoO_6. The Raman vibrations at 600 and 400 cm^{-1} are assigned to the stretching modes of the Mo-O bonds and the rocking, twisting mode in Bi_2MoO_6, respectively [49]. The vibrating peaks of Mo-O bonds for BMO and BMO-SOVs are stronger than those for F/BMO-SOVs and F/BMO, indicating that the BMO and BMO-SOVs contain more MoO_6 octahedral structures [50]. The F/BMO-SOVs and F/BMO exhibits a small peak at 885 cm^{-1}, which is attributed to the vibration of Mo-O bonds in MoO_6 [51]. The decrease in the intensities of these vibrational modes for the calcined samples suggested the deformation of the crystal structure after calcination, which could be attributed to the contribution of surface oxygen vacancies [19]. Based on the results from ESR and Raman spectra analyses, the surface

oxygen vacancies were successfully produced on the BMO-SOVs and F/BMO-SOVs via the thermal treatment process.

The UV-vis diffuse reflectance spectra of as-prepared BMO, BMO-SOVs, F/BMO-SOVs, and F/BMO are shown in **Fig. 6a** and **Fig. S2**. Compared with BMO, the absorption band edge of BMO-SOVs displayed a slight red-shift to visible region and the absorbance is enhanced in the range of 470 to 500 nm, which may be induced by surface oxygen vacancies. However, for F/BMO-SOVs, with an increasing molar ratio of Fe(III) cluster, the light absorption significantly broadens and a red-shift phenomenon occurs. From the inset of **Fig. 6a**, the color of the as-prepared photocatalysts changes from pale yellow of BMO to deep yellow of BMO-SOVs, indicating the existence of surface oxygen vacancies. In addition, the color of powder changes from deep yellow of BMO-SOVs to pale brown of F/BMO-SOVs, indicating the existence of Fe(III) clusters. The enhanced visible light absorption can be ascribed to the synergistic effect of SOVs and IFCT, as will be discussed in the following.

The band gap energy (E_g) of the semiconductors is calculated from the Kubelka-Munk equation as given below [52]:

$$\alpha h\nu = A(h\nu - E_g)^{n/2} \qquad (1)$$

where α, hν, E_g, and A are the optical absorption coefficient, photonic energy, band gap, and proportionality constant, respectively. The value of n is 1 for BMO, determined by a direct transition occurring in the semiconductor [53]. Therefore, from the plots of $(\alpha h\nu)^2$ versus energy (hν) in **Fig. 6b**, the E_g values of BMO, BMO-SOVs, and

F/BMO-SOVs can be calculated to be 2.48, 2.34, and 2.23 eV, respectively. The above results can be ascribed to the synergistic effect between SOVs and Fe(III) clusters co-modification and coupling with BMO. The valence band X-ray photoelectron spectra (VB-XPS) were used to investigate the band structure of BMO and BMO-SOVs. According to the VB XPS spectra, the binding energy of the onset edge of BMO and BMO-SOVs are found to be at 1.95 and 1.81 eV vs NHE (**Fig. 6c**), respectively. Furthermore, both BMO and BMO-SOVs exhibit the same conduction band (CB) edges, which is calculated to be -0.53 eV based on the equation of $E_{CB} = E_{VB} - E_g$ [54]. After the secondary thermal treatment, the position of VBM showed a slightly upshift for the BMO-SOVs samples, in which the VBM and CBM positions were 1.81 eV and -0.53 eV, respectively. This result can be ascribed to the introduction of SOVs on BMO could induce generated SOVs states above and partly overlapping of with the valence band (VB) which may be result in the rising of valence band maximum (VBM), thus broadening the VB width and narrowing of the band gap, as previously reported in similar spectra for other hydrogenated and thermal treated photocatalysts [20]. According to the characterization findings, a schematic illustration of the BMO band structure is provided in **Fig. 6d**.

3.3. Photocatalytic activity and Mechanism

The photocatalytic activities of as-prepared samples were evaluated by degrading phenol under visible light irradiation ($\lambda \geq 420$ nm). **Fig. 7a** and **Fig. S3a** show the variation of phenol concentration (C/C_0) over BMO, BMO-SOVs, F/BMO-SOVs, and F/BMO photocatalysts against reaction time under light irradiation. It was found that all the F/BMO-SOVs samples exhibited much better photocatalytic performances than pure BMO, in which only 4.8% of phenol was degraded. Considering F/BMO-SOVs samples, the 15% F/BMO-SOVs displayed the highest photocatalytic performance in the degradation of phenol compared to BMO, BMO-SOVs, and F/BMO. This result clearly confirms that the SOVs and IFCT effect of Fe(III) clusters act as pivotal roles for the enhanced photocatalytic performance. The optimum Fe(III) loading amount is 15% and further increasing the loading amount of Fe(III) results in a deterioration of activity, which may be ascribed to two reasons. Firstly, the increasing of Fe(III) species in the ternary photocatalyst would cause more defects, thus increasing its photocatalytic activity. Secondly, when the amount of Fe(III) clusters added was higher than 15%, the photocatalytic degradation of phenol would gradually decrease, probably due to the formation of recombination sites by excess Fe(III) clusters on the surface of Bi_2MoO_6 and the light-shielding effect of Fe(III) cluster.

Furthermore, with increasing irradiation time, the corresponding temporal UV-vis absorption spectra of photodegraded phenol with BMO, BMO-SOVs, and F/BMO-SOVs are monitored and displayed in **Fig. 7b**. At the beginning of photodegradation of phenol, the characteristic absorption peak is observed at 507 nm. With increasing irradiation time,

the absorption peak obviously decreases and virtually no peak could be observed after 180 min irradiation. This clearly demonstrates the complete photocatalytic degradation of phenol by F/BMO-SOVs during the irradiation.

In addition, in order to compare the reaction kinetics of the photodegradation process of phenol quantitatively, the degradation rates were computed using the following pseudo-first-order kinetics **Eq. (2)** [55]:

$$\ln(C_0/C) = k_{app} \cdot t \qquad (2)$$

where k_{app} denotes the apparent rate constant (min^{-1}), C_0 represents the initial phenol concentration ($mg \cdot L^{-1}$) and C represents the final concentration of phenol in solution after irradiation time t minute. The plot of $\ln(C_0/C)$ versus irradiation time (t), using BMO, BMO-SOVs, F/BMO-SOVs, and F/BMO photocatalysts, is shown in **Fig. 7c**. The results reveal that the photodegradation of phenol follows pseudo first-order kinetics model. **Fig. 7d** and **Fig. S3b** show the apparent rate constants of different samples for photodegradation of phenol. The corresponding calculated rate constants, k_{app} values are 1.94×10^{-4}, 22.4×10^{-4}, 150.3×10^{-4} and 29.2×10^{-4} min^{-1}, respectively. It can be deduced that 15% F/BMO-SOVs exhibited the highest photocatalytic activity, which is approximately 77.47 times higher than that of pure BMO. Simulated results of k_{app} for each process, in the presence of different photocatalysts with regard to phenol, were summarized in **Table S2**.

The photocatalytic degradation of phenol with different initial dosages of F/BMO-SOVs photocatalyst is shown in **Fig. S4**. It can be seen that the degradation rate

of phenol was improved accordingly, when the amount of F/BMO-SOVs was increased from 0.50 to 1.25 $g \cdot L^{-1}$, because more active sites would be provided. However, it is important to note that when the amount is more than 1.50 $g \cdot L^{-1}$, the degradation rate would inversely decrease due to the scattering of light, and would severely reduce the intensity of light penetrating through the phenol solution.

Furthermore, the total organic carbon (TOC) analysis was used to further evaluate the mineralization rate of phenol over BMO, BMO-SOVs, F/BMO-SOVs, and F/BMO under visible light illumination (**Fig. 8**). It can be observed that only 3%, 21.1%, and 32.2% of TOC were eliminated in the presence of pure BMO, BMO-SOVs, and F/BMO, respectively. In addition, the 15% F/BMO-SOVs displayed the highest TOC mineralization rate for phenol degradation compared to those of BMO, BMO-SOVs, and F/BMO. It can be seen that the F/BMO-SOVs achieved about 85.6% TOC removal efficiency within 180 min of reaction. This observation is also in accordance with the decolorization result as shown in **Fig. 7**. The TOC result of 15% F/BMO-SOVs indicates that a significant amount of phenol (85.6%) was mineralized in the photocatalytic process, which is important for practical applications of photocatalysts to avoid secondary pollution.

The practical stability of the optimized F/BMO-SOVs (15%) sample was investigated during five successive photocatalytic degradation experiments as shown in **Fig. S5a**. The photocatalytic performance shows a slight decrease after five cycles. **Fig. S5b** shows the XRD patterns of F/BMO-SOVs samples before and after

photodegradation of phenol. It was found that the crystal structure of the F/BMO-SOVs photocatalyst showed no obvious changes during the photocatalytic reaction. Consequently, the F/BMO-SOVs composite is a very stable and reusable photocatalyst, which can be utilized to degrade organic pollutants during practical applications.

PL emission has been widely used to investigate the generation, transfer, and recombination of photogenerated electron-hole pairs [31]. A low PL intensity implies a low recombination rate of free charge carriers. **Fig. 9a** shows the room-temperature PL spectra of the BMO, BMO-SOVs, F/BMO-SOVs, and F/BMO. It is clear that the PL peak intensity of BMO-SOVs is obviously lower than that of BMO, revealing the role of surface oxygen vacancies in the recombination of photogenerated charge carriers [32]. More importantly, Fe(III) clusters grafted BMO-SOVs shows the weakest photoluminescence emission intensity compared to those of BMO-SOVs and F/BMO, clearly indicating that the synergistic effect of SOVs and IFCT highly promotes efficient electron and hole separation and suppresses their recombination rate, which was further confirmed by time-resolved fluorescence decay spectra (**Fig. 9b**).

We performed time-resolved photoluminescence experiments to further investigate the recombination process of photogenerated electron-hole pairs in BMO, BMO-SOVs, F/BMO-SOVs, and F/BMO. These spectra are in good agreement with the two-exponential decay models (**Fig. 9b**). The corresponding lifetimes and intensities are also listed in **Table S3**. For F/BMO-SOVs sample, the two derived lifetimes τ_1 and τ_2 are 0.26 and 2.58 ns with the intensities of 82.7 and 17.3% of the total fluorescence intensity,

respectively. The prolonged lifetime is attributed to the synergistic effect the SOVs and the grafted Fe(III) clusters, which effectively inhibit the recombination of photogenerated electron/hole pairs. The results are in accordance with the observations from the PL measurements.

Subsequently, in order to give further evidence to confirm the separation efficiency of photogenerated charge carriers in the samples, the photocurrent generation and EIS experiments were carried out, as shown in **Fig. 9c** and **9d**. The transient photocurrent responses of BMO, BMO-SOVs, F/BMO-SOVs, and F/BMO, with several on-off cycles of visible light illumination, are displayed in **Fig. 9c**. It could be seen that 15% F/BMO-SOVs composite exhibits the highest photocurrent intensity, which is about 4.3 times stronger than that of BMO. The increase in photocurrent is attributed to the synergism of SOVs and Fe(III) clusters on BMO, which can efficiently transport photoinduced charge carriers, suppress recombination of photogenerated electrons and holes, and further confirms that the synergism system is far superior to those of BMO, BMO-SOVs, and F/BMO. The typical EIS Nyquist plots of the BMO, BMO-SOVs, F/BMO-SOVs, and F/BMO are provided in **Fig. 9d**. It is clear that the diameter of the arc radius of F/BMO-SOVs is smaller compared to other photocatalysts, implying that it possesses a stronger ability in the separation and transfer of photogenerated electron-hole pairs. Generally, the smaller radius of the arc reflects the higher efficiency of charge transfer [56]. This result further corroborates that the synergistic effect of SOVs and Fe(III) clusters on BMO can effectively enhance the separation and transfer of

photogenerated electron-hole pairs, and improve the photocatalytic activity. This result is well consistent with PL, TR-PL, and photocurrent experiments.

To further understand the underlying photocatalytic mechanism, active species trapping experiments were conducted. In general, benzoquinone (BQ), ethylenediaminetetraacetic acid disodium salt (EDTA-2Na), and isopropanol (IPA) were used as the scavengers of superoxide radicals ($\cdot O_2^-$), holes (h^+), and hydroxyl radicals ($\cdot OH$), respectively [32]. The active species trapping experiments in photocatalytic degradation of phenol with 15% F/BMO-SOVs are provided in **Fig. 10**. The trapping experiments indicate that EDTA-2Na slightly hindered the photocatalytic activity, while the addition of BQ and IPA largely suppressed the photocatalytic degradation efficiency of phenol. In addition, it was observed that only 60.02% of phenol was degraded when N_2 was conducted to reduce the dissolved O_2 in the solution, revealing that dissolved O_2 is key to the photocatalytic degradation of phenol. Thus, it could be inferred that $\cdot O_2^-$, $\cdot OH^-$ and h^+ all participated in the phenol photodegradation process over F/BMO**-**SOVs, while the $\cdot O_2^-$ species are the dominant radicals for photocatalytic degradation of phenol.

.

To further validate the reactive species and the mechanism accounting for the photocatalytic degradation of phenol, the spin-trapping ESR technique was carried out. **Fig. 11** and **Fig. S6** shows the results of BMO, BMO-SOVs, and F/BMO-SOVs. It can be seen that the characteristic ESR signal of DMPO-$\cdot O_2^-$ adduct and DMPO-$\cdot OH$ adduct

were not detectable without light irradiation. Under visible light irradiation, the $\cdot O_2^-$ and ·OH radicals signals were observed. As shown in **Fig. 11a** and **11b**, the $\cdot O_2^-$ and ·OH radicals signals is very weak in BMO, indicating that the $\cdot O_2^-$ and ·OH barely generates in the photocatalysis process. However, for F/BMO-SOVs, the intensity of the peaks increased as the irradiation time is prolonged (**Fig. 11c** and **11d**). After visible light irradiation for 12 min, we clearly observed the special spectrum with relative intensities of 1 : 1 : 1 : 1 quartet signal, which was considered to be characteristic of DMPO-$\cdot O_2^-$ adduct [57]. Meanwhile, a four-line ESR signal with relative intensities of 1 : 2 : 2 : 1 was also obtained, corresponding to the assignment of DMPO-·OH adduct [58, 59]. The ESR results indicate that $\cdot O_2^-$ and ·OH radicals are both produced in the photodegradation process over 15% F/BMO-SOVs, which are consistent with the above active species trapping experimental results. **Fig. S6** shows the DMPO-$\cdot O_2^-$ and DMPO-·OH characteristic peaks of BMO-SOVs and F/BMO. Samples BMO-SOVs and F/BMO show a highly intensive $\cdot O_2^-$ and ·OH radicals signals compared to those of BMO under visible light irradiation.

Based on the above semiconductor band structure analysis and the ESR results, herein, a synergetic mechanism of the electron-hole separation is proposed for SOVs and Fe(III) clusters on BMO, involving an IFCT process for the enhanced photocatalytic degradation of phenol under visible light (**Scheme 2**). It has been demonstrated that SOV is a shallow defect, which may be near the conduction band minimum (CBM) or above the valence band maximum (VBM) [60]. As reported by Zhao and co-authors, the band

gap of the PO_4 salt $LiTi_2(PO_4)_3$ significantly reduced due to the formation of oxygen-vacancy states above the VB, under poor oxygen conditions [61]. A similar phenomenon has also been observed on $BiPO_4$, $BiFeO_3$, and Bi_2WO_6 [19, 20, 40, 60]. Furthermore, the present experiments also showed that the photo-responsive wavelength range of BMO-SOVs is extended from 470 nm to about 505 nm (**Fig. 6a**), which may be attributed to the shallow SOVs states above and partly overlapping with the VBM of BMO, thus broadening the VB width and narrowing of the band gap. The narrowed band gap can led to an enhanced light absorption capability and would thus promoted the efficient separation of photogenerated electron-hole pairs and transfer, then leading to a dramatically enhanced photocatalytic activity [32]. In addition, the introduction of SOV only caused a slight increase of the VBM and a small narrowing of band gap for BMO and hardly any other change of the energy band structure.

To determine the position of oxygen vacancy and reveal the effect of oxygen vacancy on the band structure and photocalytic performances of BMO, density functional theory calculations have been carried, as shown Figure 6e-6g. The oxygen vacancy formation energies of Site-1, Site-2 and Site-3 are 3.45, 3.81 and 3.47 eV, respectively. Therefore, oxygen atom of BMO tends to be removed from Site-1. As shown in Fig. 6f-g, the band gap of BMO is 1.96 eV, while that of BMO-SOVs decreased to 1.84 eV. The differences of band gap between BMO and BMO-SOVs are matched, indicating that band gap of BMO decreases with the appearance of oxygen vacancies. Interestingly, the appearance of impurity state among the band gap in Figure 6g can greatly improve the

photocatalytic ability of BMO-SOVs. Furthermore, when Fe(III) clusters were grafted on the surface of BMO-SOVs, the resulting F/BMO-SOVs photocatalyst showed a very high photocatalytic activity via a synergetic effect of SOVs and Fe(III) clusters. Consequently, the enhanced photocatalytic activity for phenol degradation with F/BMO-SOVs could be explained as follows.

Under visible light irradiation, the photo-excited electrons generated from BMO-SOVs would be divided into two parts (**Eq. 3**). One part could transfer into the conduction band of BMO-SOVs. The potential for e^- (-0.53 eV vs. NHE) is more negative than $E(O_2/\cdot O_2^-)$ (-0.33 eV vs NHE, pH= 7), which could combine with the dissolved oxygen molecules (O_2) from the environment to generate $\cdot O_2^-$ radicals (**Eq. 4**). It needs to be noted that a small fraction of electrons in the CB of BMO-SOVs can easily transfer to the Fe(III) clusters owing to a more positive potential of Fe^{3+}/Fe^{2+} (0.77 eV, vs. SHE) than CB of BMO-SOVs (-0.53 eV, vs. SHE). Another part of the photo-generated electrons can directly transfer from the VB of BMO-SOVs to the Fe(III) clusters though the IFCT process. Meanwhile, the Fe(III) clusters are reduced to Fe(II) after accepting a photogenerated electron (Fe(III) + e^- = Fe(II)) (**Eq. 5**) [25, 62]. It is well known that the Fe(II) ions are unstable and easily converts back to Fe(III) via a muti-electron redox process of Fe(II) (Fe(II) + O_2 + H_2O→Fe(III) + ·OH) [63], which was also found on other cocatalysts [64]. Thus, the Fe(III) cluster provides a multi-electron redox center for oxygen reduction and Fe(III)/Fe(II) keeps a dynamic equilibrium, thereby returning to the initial states [41]. Simultaneously, the holes in the

VB of BMO-SOVs quickly migrate to its surface and react with the phenol molecules, which is partially responsible for phenol oxidation.

According to the above active species trapping experiments and EPR analysis, ·OH is the main active species and is playing key roles during the photocatalytic degradation of phenol. However, the photo-induced hole (h^+) of BMO-SOVs (1.95 eV vs. NHE) is lower than ·OH/OH^- (1.99 eV vs NHE, pH = 7) [65], thus the holes cannot directly oxidize OH^- or H_2O molecules to form ·OH radicals, which demonstrates that ·OH are not likely to be generated by the reaction. There is only one explanation that the photogenerated electrons were transferred to the Fe(III) clusters though the IFCT process and react with dissolved O_2 to generate ·O_2^- radicals. Lately, the yield of ·OH from ·O_2^- with the assistance of photoinduced electrons has been revealed (**Eqs. 6**) [66, 67]. The photocatalytic mineralization of phenol involves total transformation into CO_2 which is confirmed by TOC results in **Fig. 8** (**Eqs. 7**). Therefore, with F/BMO-SOVs catalyst, dual synergism of SOVs and grafted Fe(III) clusters greatly reduces the probability of photoinduced electron-hole recombination and shortens the electrons transmission distance, thus leading to a dramatically enhanced photocatalytic activity. Consequently, the change in k_{app} can also reflect their contribution in dual synergism. The possible reactions are described as follows:

$$\text{F/BMO-SOVs} + h\gamma \rightarrow h^+ + e^- \quad (3)$$

$$O_2 + e^- \rightarrow O_2^- \quad (4)$$

$$\text{Fe(III)} + e^- \rightarrow \text{Fe(II)} \quad (5)$$

$$O_2 + Fe(II) + H_2O \rightarrow Fe(III) + \cdot OH \quad (6)$$

$$O_2^{-}/\cdot OH/h^{+} + \text{organic compounds} \rightarrow CO_2 + H_2O \quad (7)$$

4. Conclusions

In summary, a novel F/BMO-SOVs has been rationally designed and successfully fabricated via a reliable calcination-impregnation process. The 15% F/BMO-SOVs showed the optimal efficiency of phenol degradation, reaching *ca.* 93.5% within 180 min under visible light irradiation, and the degradation rate constant was determined as nearly 80 time high as that of pure BMO. These results were further demonstrated by 85.6 % TOC removal efficiency. The dramatically enhanced photocatalytic activity is reasonably attributed to the synergistic effect between the SOVs, Fe(III) clusters and BMO. This heterojunction not only improves the visible light absorption, but also produces the direct interfacial charge transfer (IFCT) from the SOVs isolated states to the surface Fe(III) clusters, which significantly promotes the separation and migration of photogenerated electrons and holes, and simultaneously suppresses the recombination of electrons and holes, thus resulting in the high photocatalytic performance on F/BMO-SOVs. In addition, this work not only provides a synergistic effect between SOVs, Fe(III) clusters and BMO involving an IFCT process for charge generation and separation, but also provides a new approach to fabricating active photocatalysts for environmental remediation and other applications.

Acknowledgements

This work was supported by the National Natural Science Foundation of China (No. 21663030, 21666039) and the Project of Science & Technology Office of Shaanxi Province (No. 2018TSCXL-NY-02-01, 2015SF291, 2013K11-08, 2013SZS20-P01) and Natural Science Program of the Education Department of Shaanxi Province (No. 15JS119).

References

[1] P. Lisowski, J. C. Colmenares, O. Mašek, W. Lisowski, D. Lisovytskiy, A. Kamińska, D. Łomot, ACS Sustainable Chem. Eng. 5 (2017) 6274-6287.

[2] E. Grabowska, J. Reszczynska, A. Zaleska, Water Res. 46 (2012) 5453-5471.

[3] D. Fabbri, A. B. Prevot, E. Pramauro, Appl. Catal. B: Environ. 62 (2006) 21-27.

[4] A. K. L. Sajjad, S. Shamaila, B. Tian, F. Chen, J. Zhang, Appl. Catal. B: Environ. 91 (2009) 397-405.

[5] V. Vaianoa, M. Matarangoloa, J. J. Murciab, H. Rojasb, J. A. Navíoc, M. C. Hidalgoc, Appl. Catal. B: Environ. 225 (2018) 197-206.

[6] G. H. Tian, Y. J. Chen, R. T. Zhai, J. Zhou, W. Zhou, R. H. Wang, K. Pan, Ch. G. Tian, H. G. Fu, J. Mater. Chem. A 1 (2013) 6961-6968.

[7] W. Wei, Y. Dai, B. B. Huang, J. Phys. Chem. C 113 (2009) 5658-5663.

[8] L. W. Zhang, T. G. Xu, X. Zhao, Y. F. Zhu, Appl. Catal. B: Environ. 98 (2010) 138-146.

[9] X. X. Chang, T. Wang, P. Zhang, J. J. Zhang, A. Li, J. L. Gong, J. Am. Chem. Soc. 137 (2015) 8356-8359.

[10] Z. Dai, F. Qin, H. P. Zhao, J. Ding, Y. L. Liu, R. Chen, ACS Catal. 6 (2016) 3180-3192.

[11] Z. Y. Zhao, Y. Zhou, F. Wang, K. H. Zhang, S. Yu, K. Cao, ACS Appl. Mater. Interfaces 7 (2015) 730-737.

[12] S. J. Tan, Y. F. Ji, Y. Zhao, A. D. Zhao, B. Wang, J. L. Yang, J. G. Hou, J. Am. Chem. Soc. 133 (2011) 2002-2009.

[13] X. Y. Xiao, J. Jing, L. Z. Zhang, Appl. Catal. B: Environ. 142-143 (2013) 487-493.

[14] G. Zhang , Z. Y. Hu , M. Sun , Y. Liu , L. M. Liu , H. J. Liu, C. P. Huang, J. H. Qu, J. H. Li, Adv. Funct. Mater. 25 (2015) 3726-3734.

[15] K. Zhao, L. Z. Zhang, J. J. Wang, Q. X. Li, W. W. He, J. J. Yin, J. Am. Chem. Soc. 135 (2013) 15750-15753.

[16] H. Hirakawa, M. Hashimoto, Y. Shiraishi, T. Hirai, J. Am. Chem. Soc. 139 (2017) 10929-10936.

[17] H. Li, J. Shang, Z. H. Ai, L. Z. Zhang, J. Am. Chem. Soc. 137 (2015) 6393-6399.

[18] S. C. Wang, P. Chen, Y. Bai, J. H. Yun, G. Liu, L. Z. Wang, Adv. Mater. 30 (2018) 1800486.

[19] Z. Wei, Y. F. Liu, J. Wang, R. L. Zong, W. Q. Yao, J. Wang, Y. F. Zhu, Nanoscale 7 (2015) 13943-13950.

[20] D. Chen, F. Niu, L. S. Qin, S. Wang, N. Zhang, Y. X. Huang, Sol. Energy Mater. Sol. Cells 171 (2017) 24-32.

[21] Y. Q. Wu, G. X. Lu, Phys. Chem. Chem. Phys. 16 (2014) 4165-4175.

[22] Y. Nosaka, S. Takahashi, H. Sakamoto, A. Y. Nosaka, J. Phys. Chem. C 115 (2011) 21283-21290.

[23] X. Q. Qiu, M. Miyauchi, K. Sunada, M. Minoshima, M. Liu, Y. Lu, D. Li, Y. Shimodaira, Y. Hosogi, Y. Kuroda, K. Hashimoto, ACS Nano 6 (2012) 1609-1618.

[24] H. G. Yu, H. Irie, K. Hashimoto, J. Am. Chem. Soc. 132 (2010) 6898-6899.

[25] M. Liu, X. Q. Qiu, M. Miyauchi, K. Hashimoto, J. Am. Chem. Soc. 135 (2013) 10064-10072.

[26] M. Liu, R. Inde, M. Nishikawa, X. Q. Qiu, D. Atarashi, E. Sakai, Y. Nosaka, K. Hashimoto, M. Miyauchi, ACS Nano 8 (2014) 7229-7238.

[27] Q. Liu, T. X. Chen, Y. R. Guo, Z. G. Zhang, X. M. Fang, Appl. Catal. B: Environ. 205 (2017) 173-181.

[28] H. G. Yu, W. Y. Chen, X. F. Wang, Y. Xu, J. G. Yu, Appl. Catal. B: Environ. 187 (2016) 163-170.

[29] W. B. Sun, H. Y. Zhang, J. Lin, J. Phys. Chem. C 118 (2014) 17626-17632.

[30] C. J. Huang, J. L. Hu, S. Cong, Z. G. Zhao, X. Q. Qiu, Appl. Catal. B: Environ. 174-175 (2015) 105-112.

[31] X. Feng, W. D. Zhang, Y. J. Sun, H. W. Huang, F. Dong, Environ. Sci.: Nano 4 (2017) 604-612.

[32] D. J. Wang, H. D. Shen, L. Guo, C. Wang, F. Fu, Y. C. Liang, Appl. Surf. Sci. 436 (2018) 536-547.

[33] Z. H. Yuan, J. H. Jia, L. D. Zhang, Mat. Chem. Phys. 73 (2002) 323-326.

[34] G. Kresse, J. Hafner, Phys. Rev. B 47 (1993) 558-561.

[35] J. P. Perdew, K. Burke, M. Ernzerhof, Phys. Rev. Lett. 78 (1997) 1396-1396.

[36] H. J. Monkhorst, J. D. Pack, Phys. Rev. B 13 (1976) 5188-5192.

[37] W. Zhao, C. Li, A. J. Wang, C. C. Lv, W. H. Zhu, S. P. Dou, Q. Wang, Q. Zhong, Phys. Chem. Chem. Phys. 19 (2017) 28696-28709.

[38] J. H. Guo, L. Shi, J. Y. Zhao, Y. Wang, K. B. Tang, W. Q. Zhang, C. Z. Xie, X. Y. Yuan, Appl. Catal. B: Environ. 224 (2018) 692-704.

[39] Y. S. Xu, W. D. Zhang, Dalton Trans. 42 (2013) 1094-1101.

[40] Y. H. Lv, W. Q. Yao, R. L. Zong, Y. F. Zhu, Sci. Rep. 6 (2016) 19347.

[41] H. G. Yu, H. Irie, Y. Shimodaira, Y. Hosogi, Y. Kuroda, M. Miyauchi, K. Hashimoto, J. Phys.

Chem. C 11 (2010) 16481-16487.

[42] H. G. Yu, G. Q. Cao, F. Chen, X. F. Wang, J. G. Yu, M. Lei, Appl. Catal. B: Environ. 160-161 (2014) 658-665.

[43] S. Q. Liu, P. P. Deng, G. P. Dai, Y. Liang, S. Y. Zhang, Ceram. Int. 42 (2016) 10094-10098.

[44] Y. Ma, Y. L. Jia, Z. B. Jiao, M. Yang, Y. X. Qi, Y. P. Bi, Chem. Commun. 51 (2015) 6655-6658.

[45] C. Zhang, Y. F. Zhu, Chem. Mater. 17 (2005) 3537-3545.

[46] J. G. Hou, S. Y. Cao, Y. Z. Wu, F. Liang, Y. F. Sun, Z. S. Lin, L. C. Sun, Nano Energy 32 (2017) 359-366.

[47] W. T. Bi, C. M. Ye, C. Xiao, W. Tong, X. D. Zhang, W. Shao, Y. Xie, Small 10 (2014) 2820-2825.

[48] H. Li, J. Li, Z. H. Ai, F. L. Jia, L. Z. Zhang, Angew. Chem. Int. Ed. 57 (2018) 122-138.

[49] H. B. Fu, C. S. Pan, W. Q. Yao, Y. F. Zhu, J. Phys. Chem. B 109 (2005) 22432-22439.

[50] Z. X. Yang, M. Shen, K. Dai, X. H. Zhang, H. Chen, Appl. Surf. Sci. 430 (2018) 505-514.

[51] R. Murugan, Physica B 352 (2004) 227-232.

[52] Z. Wan, G. K. Zhang, X. Y. Wu, S. Yin, Appl. Catal. B: Environ. 207 (2017) 17-26.

[53] D. J. Wang, H. D. Shen, L. Guo, F. Fu, Y. C. Liang, New J. Chem. 40 (2016) 8614-8624.

[54] Q. Wang, W. Wang, L. L. Zhong, D. M. Liu, X. Z. Cao, F. Y. Cui, Appl. Catal. B: Environ. 220 (2018) 290-302.

[55] C. W. Tan, G. Q. Zhu, M. Hojamberdiev, K. Okada, J. Liang, X. C. Luo, P. Liu, Appl. Catal. B: Environ. 152-153 (2014) 425-436.

[56] X. J. Bai, L. Wang, R. L. Zong, Y. H. Lv, Y. Q. Sun, Y. F. Zhu, Langmuir 29 (2013) 3097-3105.

[57] W. W. He, H. M. Jia, W. G. Wamer, Z. Zheng, P. J. Li, J. H. Callahan, J. J. Yin, J. Catal. 320 (2014) 97-105.

[58] P. X. Qiu, C. M. Xu, H. Chen, F. Jiang, X. Wang, R. F. Lu, X. R. Zhang, Appl. Catal. B: Environ. 206 (2017) 319-327.

[59] P. H. Shao, Z. J. Ren, J. Y. Tian, S. S. Gao, X. B. Luo, W. X. Shi, B. Y. Yan, J. Li, F. Y. Cui, Chem. Eng. J. 323 (2017) 64-73.

[60] Y. H. Lv, Y. Y. Zhu, Y. F. Zhu, J. Phys. Chem. C 117 (2013) 18520-18528.

[61] L. J. Chen, Y. J. Zhao, J. Y. Luo, Y. Y. Xia, Phys. Lett. A 375 (2011) 934-938.

[62] M. Nishikawa, Y. Mitani, Y. Nosaka, J. Phys. Chem. C 116 (2012) 14900-14907.

[63] M. Miyauchi, H. Irie, M. Liu, X. Q. Qiu, H. G. Yu, K. Sunada, K. Hashimoto, J. Phys. Chem. Lett. 7 (2015) 75-84.

[64] Y. Nosaka, S. Takahashi, Y. Mitani, X. Qiu, M. Miyauchi, Appl. Catal., B: Environ. 111-112 (2012) 636-640.

[65] X. L. Hu, J. Tian, Y. J. Xue, Y. J. Li, H. Z. Cui, ChemCatChem 9 (2017) 1511-1516.

[66] S. M. Sun, W. Z. Wang, L. Zhang, L. Zhou, W. Z. Yin, M. Shang, Environ. Sci. Technol. 43 (2009) 2005-2010.

[67] B. Yuan, C. H. Wang, Y. Qi, X. L. Song, K. Mu, P. Guo, L. T. Meng, H. M. Xi, Colloids and Surfaces A: Physicochem. Eng. Aspects 425 (2013) 99-107.

Figures captions

Fig. 1 (a) XRD patterns of samples BMO, BMO-SOVs, F/BMO-SOVs, and F/BMO, (b) Enlarged XRD patterns in a 2Theta range of 26 - 31°, (c) XPS spectra of Bi 4f, and (d) XPS spectra of O 1s for samples BMO, BMO-SOVs, and F/BMO-SOVs.

Fig. 2 FE-SEM images of as-prepared BMO (a, b), and F/BMO-SOVs composites (c, d).

Fig. 3 The corresponding EDS elemental mapping images of (a) Bi, (b) Mo, (c) O, and (d) Fe in sample F/BMO-SOVs.

Fig. 4 TEM and HR-TEM images of BMO (a, b), and F/BMO-SOVs composites (c, d).

Fig. 5 HR-TEM images of (a) BMO and (b) BMO-SOVs, (c) EPR spectra of BMO, BMO-SOVs, F/BMO-SOVs, and F/BMO at 77 K, (d) Raman spectra of BMO, BMO-SOVs, F/BMO-SOVs, and F/BMO.

Fig. 6 (a)UV-vis diffuse reflectance spectra of BMO, BMO-SOVs, F/BMO-SOVs, and F/BMO (inset: the color of the photocatalysts), (b) The band gap value, estimated by a related curve of $(\alpha h\nu)^2$ versus photon energy plotted, (c) Valence band XPS spectra, and (d) Schematic illustration of BMO and BMO-SOVs band structure, (e) The optimized configuration and oxygen vacancy sites of BMO (The violet, dark green and red spheres represent Bi, Mo and O atoms, respectively.), (f) Band structures of BMO and BMO-SOVs, (g) The Femi level is set to zero.

Fig. 7 (a) photocatalytic degradation efficiency of phenol by BMO, BMO-SOVs, F/BMO-SOVs, and F/BMO, (b) The absorption spectra of phenol during

photodegradation under visible light using BMO, BMO-SOVs, and F/BMO-SOVs, respectively, (c) Kinetic plots of C/C_0 versus irradiation time for the photodegradation of phenol with different catalysts, (d) The photodegradation rate constants of phenol using different catalysts.

Fig. 8 TOC removal of phenol over BMO, BMO-SOVs, F/BMO-SOVs, and F/BMO composites under visible light illumination.

Fig. 9 (a) Photoluminescence spectra, (b) Time-resolved fluorescence decay spectra, (c) Transient photocurrent response under visible light irradiation, and (d) Electrochemical impedance spectroscopy (EIS) of BMO, BMO-SOVs, F/BMO-SOVs, and F/BMO.

Fig. 10 Comparison of the effect of different radical scavengers during photocatalytic degradation of phenol with 15% F/BMO-SOVs composite under visible light irradiation ($\lambda \geq 420$ nm).

Fig. 11 DMPO spin-trapping ESR spectra of (a) BMO and (c) 15% F/BMO-SOVs in methanol dispersion for DMPO-$\cdot O_2^-$. DMPO spin-trapping ESR spectra of (b) BMO and (d) 15% F/BMO-SOVs in aqueous dispersion for DMPO-$\cdot$OH.

Scheme 1 Schematic illustration of the preparation process of F/BMO-SOVs samples.

Scheme 2 Schematic diagram illustrating the proposed degradation mechanism of organic pollutants over 15% F/BMO-SOVs photocatalysts under visible light irradiation ($\lambda \geq 420$ nm).

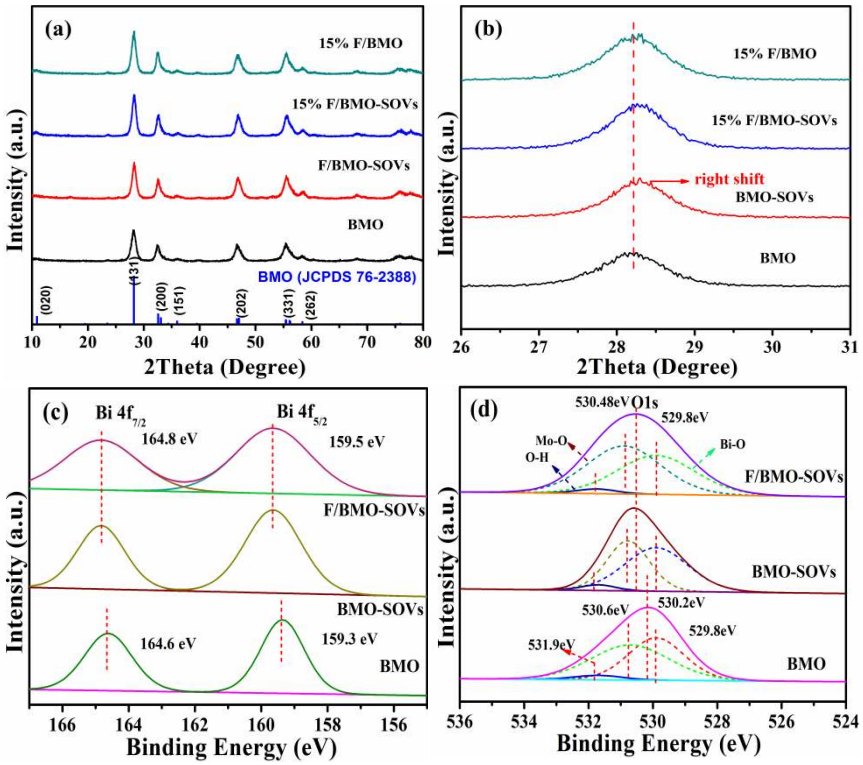

Fig. 1 (a) XRD patterns of samples BMO, BMO-SOVs, F/BMO-SOVs, and F/BMO, (b) Enlarged XRD patterns in a 2Theta range of 26 - 31°, (c) XPS spectra of Bi 4f, and (d) XPS spectra of O 1s for samples BMO, BMO-SOVs, and F/BMO-SOVs.

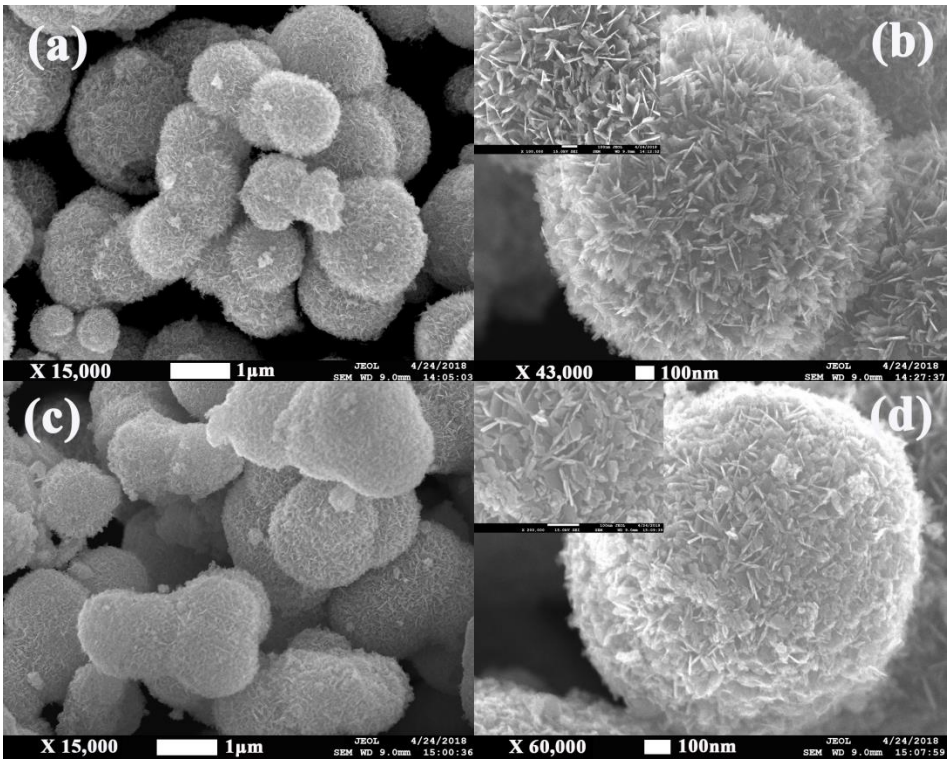

Fig. 2 FE-SEM images of as-prepared BMO (a, b), and F/BMO-SOVs composites (c, d).

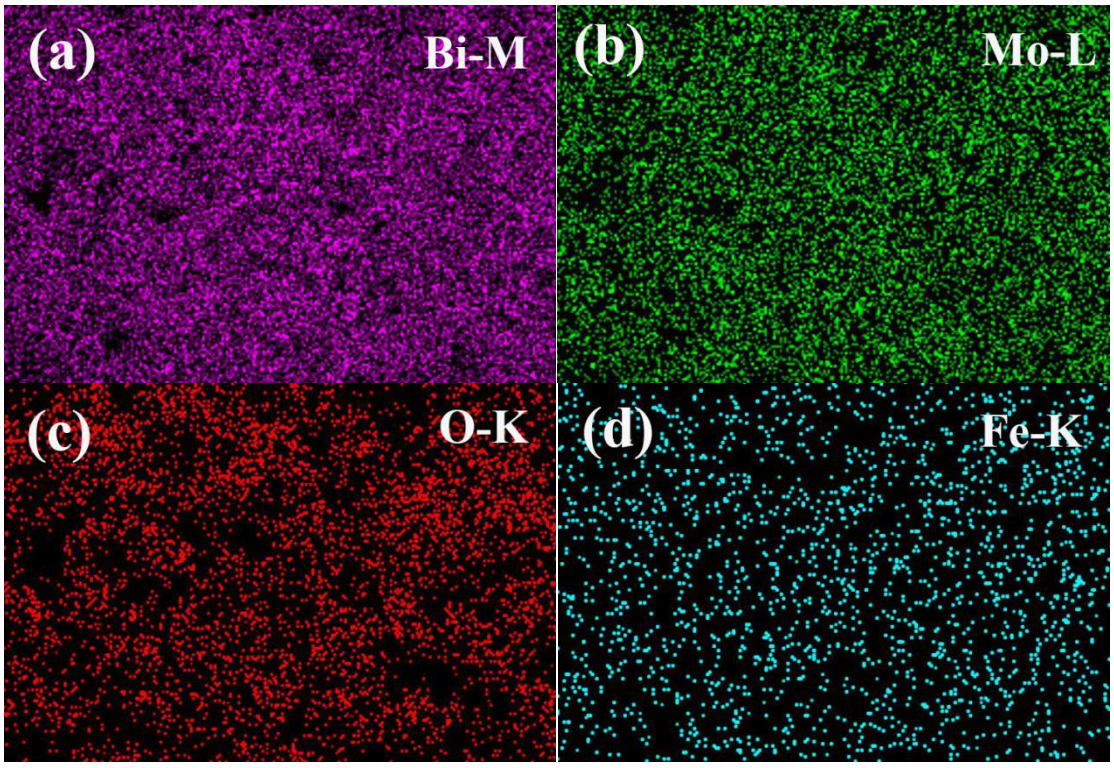

Fig. 3 The corresponding EDS elemental mapping images of (a) Bi, (b) Mo, (c) O, and (d) Fe in sample F/BMO-SOVs.

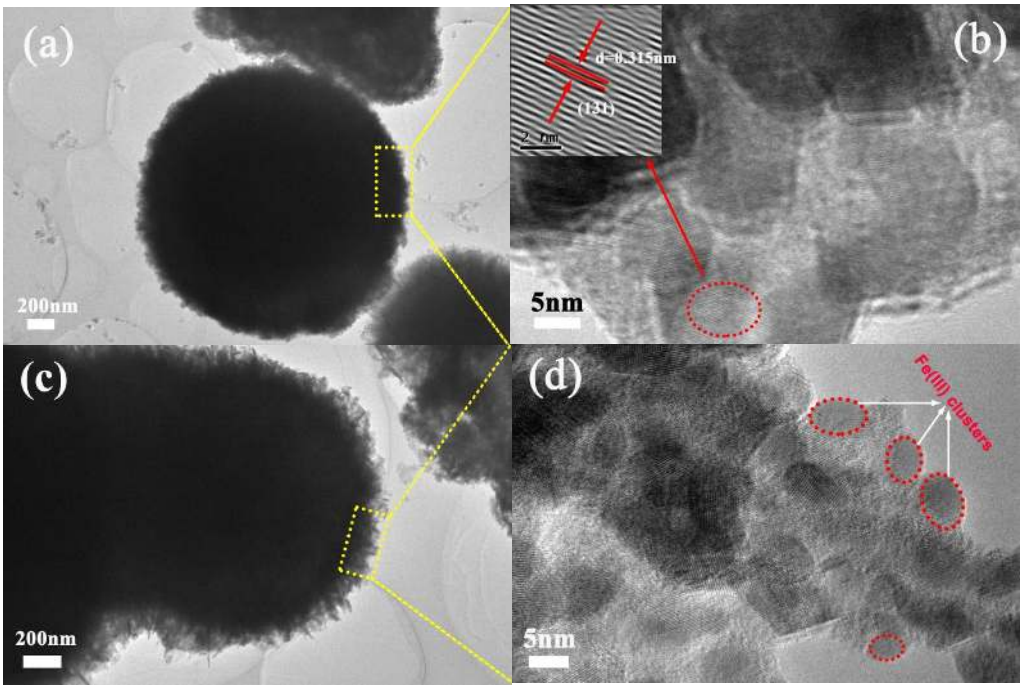

Fig. 4 TEM and HR-TEM images of BMO (a, b), and F/BMO-SOVs composites (c, d).

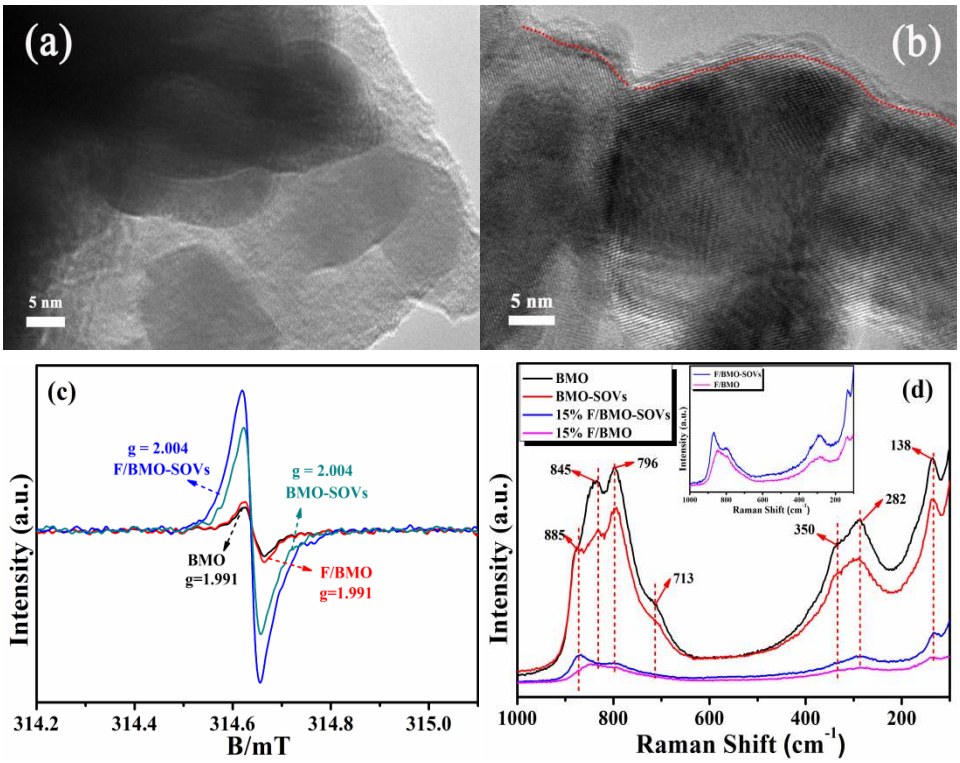

Fig. 5 HR-TEM images of (a) BMO and (b) BMO-SOVs; (c) EPR spectra of BMO, BMO-SOVs, F/BMO-SOVs, and F/BMO at 77 K; (d) Raman spectra of BMO, BMO-SOVs, F/BMO-SOVs, and F/BMO.

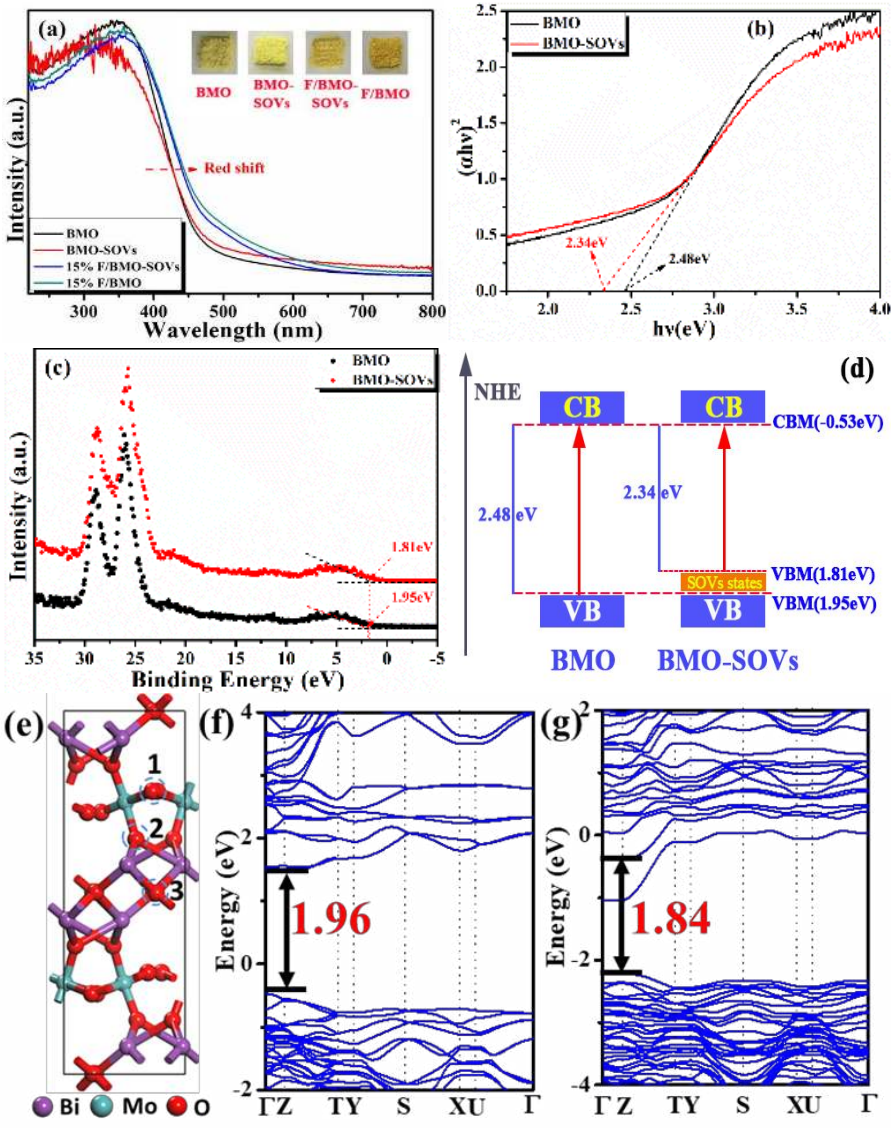

Fig. 6 (a)UV-vis diffuse reflectance spectra of BMO, BMO-SOVs, F/BMO-SOVs, and F/BMO (inset: the color of the photocatalysts), (b) The band gap value, estimated by a related curve of $(\alpha h\nu)^2$ versus photon energy plotted, (c) Valence band XPS spectra, and (d) Schematic illustration of BMO and BMO-SOVs band structure, (e) The optimized configuration and oxygen vacancy sites of BMO (The violet, dark green and red spheres represent Bi, Mo and O atoms, respectively.), (f) Band structures of BMO and BMO-SOVs, (g) The Femi level is set to zero.

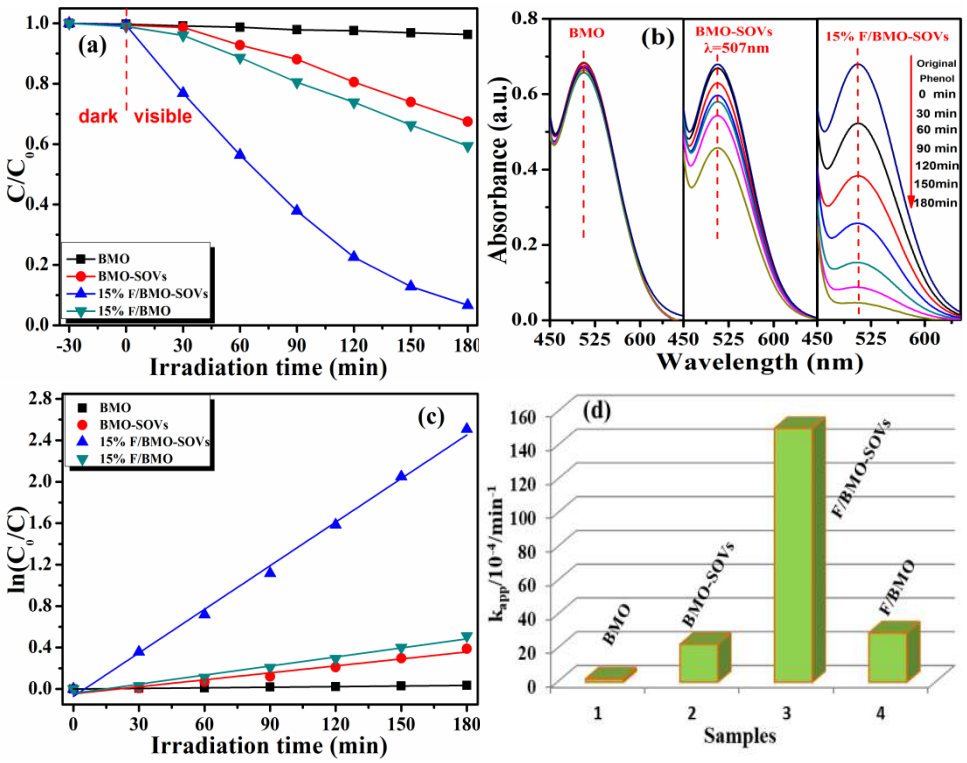

Fig. 7 (a) Photocatalytic degradation efficiency of phenol by BMO, BMO-SOVs, F/BMO-SOVs, and F/BMO, (b) The absorption spectra of phenol during photodegradation under visible light using BMO, BMO-SOVs, and F/BMO-SOVs, respectively, (c) Kinetic plots of C/C_0 versus irradiation time for the photodegradation of phenol with different catalysts, (d) The photodegradation rate constants of phenol using different catalysts.

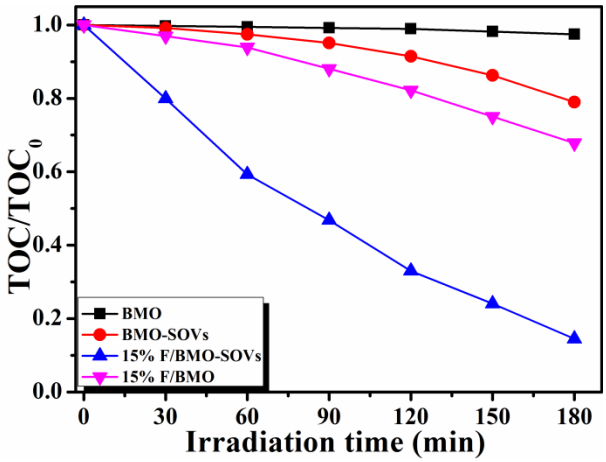

Fig. 8 TOC removal of phenol over BMO, BMO-SOVs, F/BMO-SOVs, and F/BMO composites under visible light illumination.

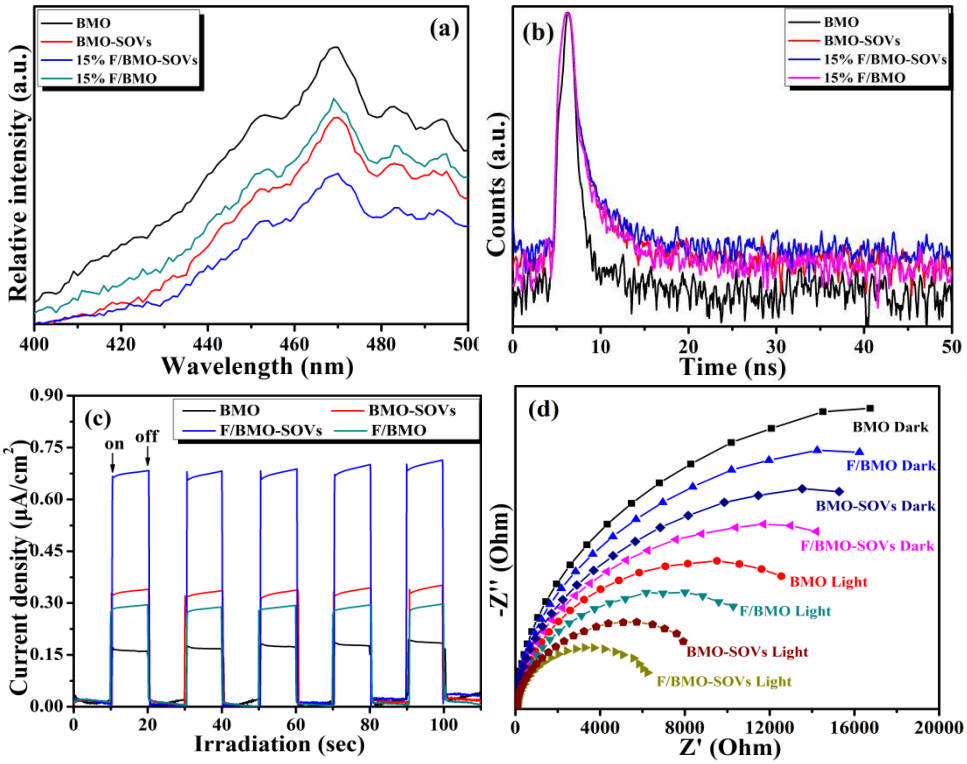

Fig. 9 (a) Photoluminescence spectra, (b) Time-resolved fluorescence decay spectra, (c) Transient photocurrent response under visible light irradiation, and (d) Electrochemical impedance spectroscopy (EIS) of BMO, BMO-SOVs, F/BMO-SOVs, and F/BMO.

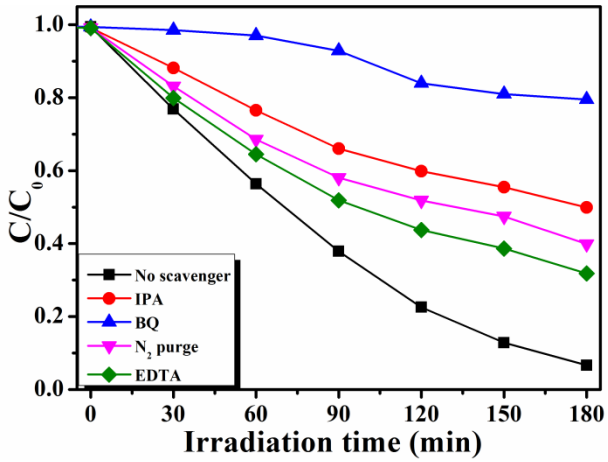

Fig. 10 Comparison of the effect of different radical scavengers during photocatalytic degradation of phenol with 15% F/BMO-SOVs composite under visible light irradiation ($\lambda \geq 420$ nm).

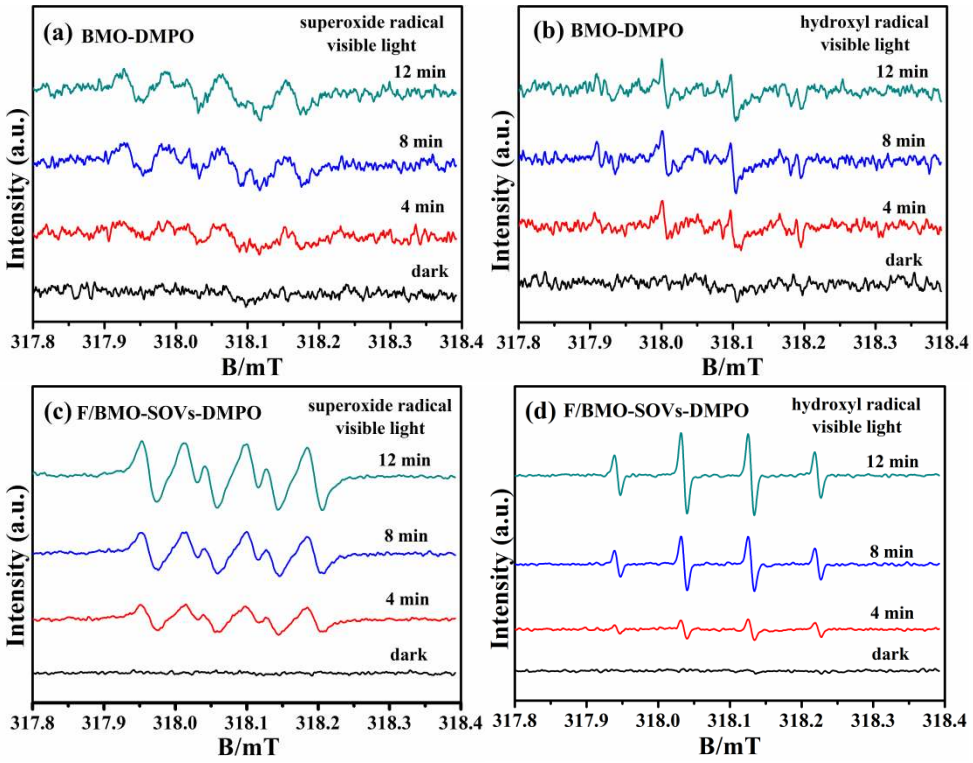

Fig. 11 DMPO spin-trapping ESR spectra of (a) BMO and (c) 15% F/BMO-SOVs in methanol dispersion for DMPO-·O_2^-. DMPO spin-trapping ESR spectra of (b) BMO and (d) 15% F/BMO-SOVs in aqueous dispersion for DMPO-·OH.

Scheme captions

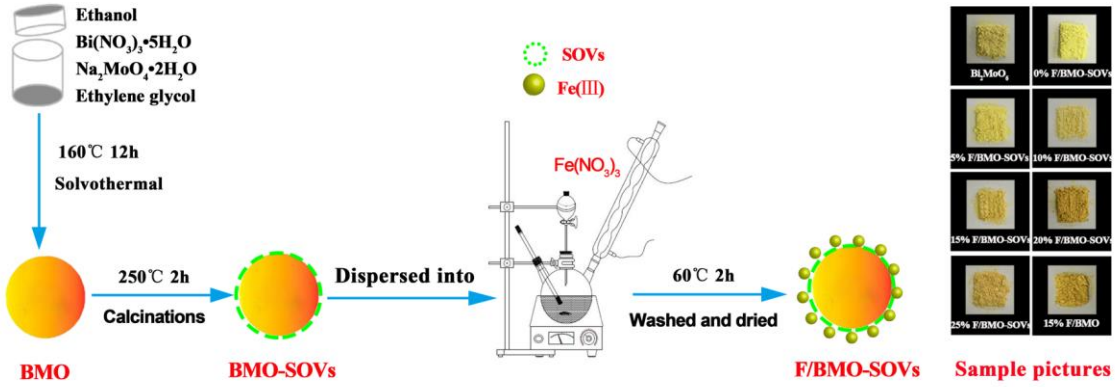

Scheme 1 Schematic illustration of the preparation process of F/BMO-SOVs samples.

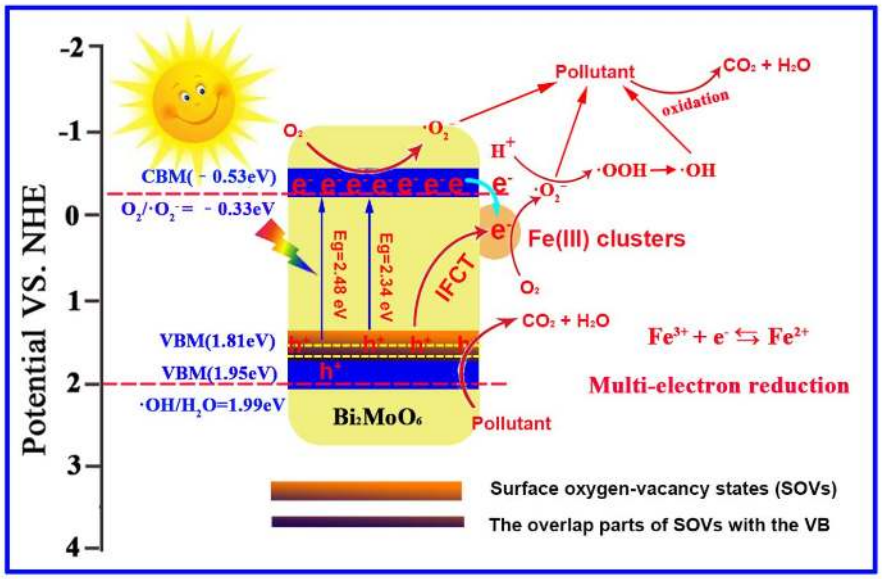

Scheme 2 Schematic diagram illustrating the proposed degradation mechanism of organic pollutants over 15% F/BMO-SOVs photocatalysts under visible light irradiation ($\lambda \geq 420$ nm).